Computational Study of Nozzle Configuration Effects on Heat Transfer and Flow Characteristics in Aero-Engine Swirling Anti-Icing Systems

Yi Tu[1,*], Yuan Wu[2], Bin Zeng[1], Songrong Luo[1], Wen Liu[1] and Yu Zeng[3]

[1] Hunan Engineering Research Center for Numerical Simulation Technology of Aerospace Thermal Fluid Systems, Hunan University of Arts and Science, Changde, 415000, China

[2] Liaoning Provincial Key Laboratory of Aircraft Ice Protection, AVIC Aerodynamics Research Institute, Shenyang, 110034, China

[3] School of Aeronautic Science and Engineering, Beihang University, Beijing, 100191, China

INFORMATION

Keywords:
Swirl anti-icing
heat transfer
aero-engine
hot and cold spots
nozzle configuration

DOI: 10.23967/j.rimni.2025.10.70253

SCIPEDIA Revista Internacional de Métodos Numéricos para Cálculo y Diseño en Ingeniería

Revista Internacional Métodos numéricos para cálculo y diseño en ingeniería RIMNI in cooperation with CIMNE

Computational Study of Nozzle Configuration Effects on Heat Transfer and Flow Characteristics in Aero-Engine Swirling Anti-Icing Systems

Yi Tu[1,*], Yuan Wu[2], Bin Zeng[1], Songrong Luo[1], Wen Liu[1] and Yu Zeng[3]

[1]Hunan Engineering Research Center for Numerical Simulation Technology of Aerospace Thermal Fluid Systems, Hunan University of Arts and Science, Changde, 415000, China

[2]Liaoning Provincial Key Laboratory of Aircraft Ice Protection, AVIC Aerodynamics Research Institute, Shenyang, 110034, China

[3]School of Aeronautic Science and Engineering, Beihang University, Beijing, 100191, China

ABSTRACT

Engine inlet icing persists as a critical hazard to aviation operational safety, compromising aerodynamic performance and potentially inducing catastrophic engine failure. Aero-engine swirling anti-icing systems inject high-temperature bleed air into an annular chamber at the engine's leading edge through tangentially positioned nozzles. This high-velocity jet entrains low-temperature air within the chamber, establishing a circulatory flow that effectively heats the lip surface to prevent ice formation. This study employs computational fluid dynamics (CFD) method to systematically evaluate the flow and heat transfer characteristics of four distinct nozzle configurations within an aero-engine anti-icing chamber: conical single-orifice, diffuser-equipped, elliptical dual-orifice, and elliptical quad-orifice nozzles. Results indicate that the conical single-orifice nozzle exhibits the highest entrainment efficiency due to its concentrated jet structure, whereas the diffuser-equipped nozzle demonstrates 16.4%–18.1% lower efficiency, attributable to premature kinetic energy dissipation. At identical bleed air flow rates, the diffuser-equipped nozzle yields the lowest circulation velocity and pressure loss, necessitating minimal bleed air pressure. The elliptical quad-orifice nozzle optimally mitigates hot and cold spots via multi-jet energy dispersion, achieving a maximum 34.7% reduction in lip surface temperature differentials compared to the conical single-orifice design within the analyzed bleed air mass flow rate range. Nozzle configurations exert limited influence on the average Nusselt number, with a maximum relative deviation of 5.48% observed across all nozzle configurations when compared to established empirical correlations.

OPEN ACCESS

Received: 11/07/2025

Accepted: 21/08/2025

Published: 15/12/2025

DOI
10.23967/j.rimni.2025.10.70253

Keywords:
Swirl anti-icing
heat transfer
aero-engine
hot and cold spots
nozzle configuration

*Correspondence: Yi Tu (tuyi.huas@outlook.com).

1 Introduction

Aircraft engine icing remains a critical threat to aviation safety. Icing on the inlet lip surface of the aero-engine is primarily caused by the impingement of supercooled water droplets and low ambient temperatures, which can alter the engine's aerodynamic profile, lead to performance degradation, and even trigger catastrophic engine shutdowns [1]. To combat this hazard, researchers have developed diverse anti-icing methodologies, including mechanical de-icing [2], electro-impulse ice protection systems [3,4], hot air anti-icing technology (HAI) [5,6], and hybrid approaches integrating superhydrophobic coatings with electrothermal heating [7,8]. Among these solutions, HAI technology has emerged as the most widely adopted due to its inherent reliability and technical maturity—particularly for the aero-engine inlet, where stringent anti-icing requirements and substantial energy density demands necessitate robust performance. The HAI system for aero-engines directly utilizes the bleed air from engines (near the air source), eliminating the need for extensive pipeline infrastructure while delivering dual advantages in anti-icing performance and system weight optimization. Therefore, in the foreseeable future, HAI will remain the optimal solution for aero-engine anti-icing technology [9].

The piccolo tube system remains the prevailing hot-air anti-icing solution for most modern aircraft engine inlets. These tubes are circumferentially positioned within the annular chamber featuring a D-shaped cross-section (termed the D-chamber) at the leading edge of the aircraft engine. They discharge high-temperature bleed air onto the inner walls of the D-chamber, heating the engine inlet lip surface and preventing ice formation [10,11]. In 1985, Rosenthal proposed a swirl hot air anti-icing (SHAI) scheme for engine inlets wherein high-velocity hot air is injected tangentially through nozzles into the D-chamber. This configuration generates a high-speed circumferential swirl flow within the D-chamber, facilitating intense heat transfer between the swirling hot air and the inner wall. Compared to the traditional piccolo tube system, this SHAI system offers similar anti-icing performance while featuring a leaner configuration and reduced weight [12,13].

In SHAI systems, improving anti-icing efficiency primarily depends on the appropriate design of nozzles and the optimization of airflow parameters. Chilukuri validated through numerical simulations and water tunnel experiments that SHAI technology can effectively prevent engine inlet icing [14]. Ismail's study revealed that adjusting nozzle rotation angles and geometries can significantly improve the performance of the SHAI system and reduce system energy consumption [15]. Anderson's comparative study found that SHAI systems achieve anti-icing performance comparable to that of the piccolo tube anti-icing system while significantly reducing weight [16]. Liu et al. conducted a comparative study on impinging jets, offset jets, and swirling jets for wing anti-icing applications. Their findings revealed that swirling-jet configurations can enhance internal heat transfer, increase vortex intensity, and improve circumferential velocity, though this comes with an increase in internal pressure loss compared with traditional impinging jet designs [17].

Following the proposal and validation of the SHAI concept, companies such as Rohr Inc. and General Electric have sought to optimize the swirl flow field within the D-chamber by redesigning nozzle structures and modifying jet configurations. Mark et al. designed jet nozzle with helical channels for the SHAI system [18]; Michael proposed a scheme involving multiple serially arranged elliptical nozzles [19]; Radhakrishna added a plurality of spaced circumferentially arranged tabs at the nozzle outlet to generate vortices and enhance mixing [20]; Joel et al. proposed jet nozzles with a central diffuser element [21]. However, the impact of nozzle configurations on internal flow and heat transfer performance of the D-chamber remains understudied. Swirl anti-icing technology has demonstrated its potential value in anti-icing applications for aero-engine inlets, but further research is needed to optimize its performance and control energy consumption.

Flight tests [22], wind tunnel experiments [23,24], and numerical simulations are the primary design and verification methods for current aircraft HAI systems. In recent years, with the advancement of computer technology, CFD methods have been widely applied in the research of aircraft anti-icing systems due to its advantages in analysis efficiency and cost. Croce et al. conducted 3D thermal analysis using FENSAP-ICE to study the impact of piccolo tube design parameters on the flow and heat transfer performance in the anti-icing chamber [25]. Ismail et al. improved the Brown correlation equation through CFD and adapted it to the nacelle anti-icing system at different environmental temperatures [26]. Bu et al. [27] and Yang et al. [28] adopted the tight-coupling CFD method to conduct optimization research on the piccolo tube-type wing anti-icing system. Numerous studies have demonstrated that CFD methods have become an efficient and reliable approach for the design and development of aviation anti-icing systems [29].

Traditional SHAI systems inject high-temperature air at high velocity into the annular engine anti-icing chamber via single-hole nozzles. This configuration causes insufficient mixing between the injected air and the ambient air. In this curved chamber, the high-velocity hot-air jet tends to directly impinge on the chamber walls, generating large-area hot spots on the lip surface, which may induce significant thermal stresses in structural materials. The high-velocity jet entrains the local fluid, causing it to circulate within the D-chamber at a flow rate several times that of the bleed air. This enhanced convective motion effectively heats the lip surface. However, the circulating flow in such annular channels is typically accompanied by significant centrifugal effects. The centrifugal forces deflect the high-velocity mainstream toward the outer-ring side wall, creating a low-velocity region near the inner-ring side wall with even a risk of flow separation. This results in significantly lower heat transfer intensity on the inner wall compared to the outer wall, forming cold spots on the lip surface, and increasing the risk of local ice formation. Geometric optimization of the nozzle is a key approach to suppressing the hot and cold spot issues on the surface of the anti-icing chamber. This study aims to systematically assess the impact of nozzle configurations on the internal flow and heat transfer characteristics within aero-engine SHAI systems. The primary objective is to develop effective nozzle optimization strategies that enhance flow and thermal performance in SHAI systems.

2 Numerical Methodology

CFD simulations are conducted to evaluate four nozzle configurations, namely the diffuser-equipped nozzle, conical single-orifice nozzle, elliptical dual-orifice nozzle, and elliptical quad-orifice nozzle, by comparing their effects on injection efficiency, heat transfer characteristics, and hot/cold spot distribution on the engine inlet lip surface.

2.1 Physical Model and Boundary Conditions

This study focuses on the annular anti-icing chamber located at the leading edge of the aero-engine inlet, as shown in Fig. 1. High-pressure and high-temperature bleed air from the engine is injected through a nozzle into the annular chamber. The injected high-velocity air entrains ambient surrounding air, generating a circulating swirl flow within the D-chamber and heating the lip surface of the engine inlet. This flow circulates in the D-chamber at a flow rate several times that of the bleed air, and the exhaust is discharged through the outlet port after completing the cyclic heat exchange.

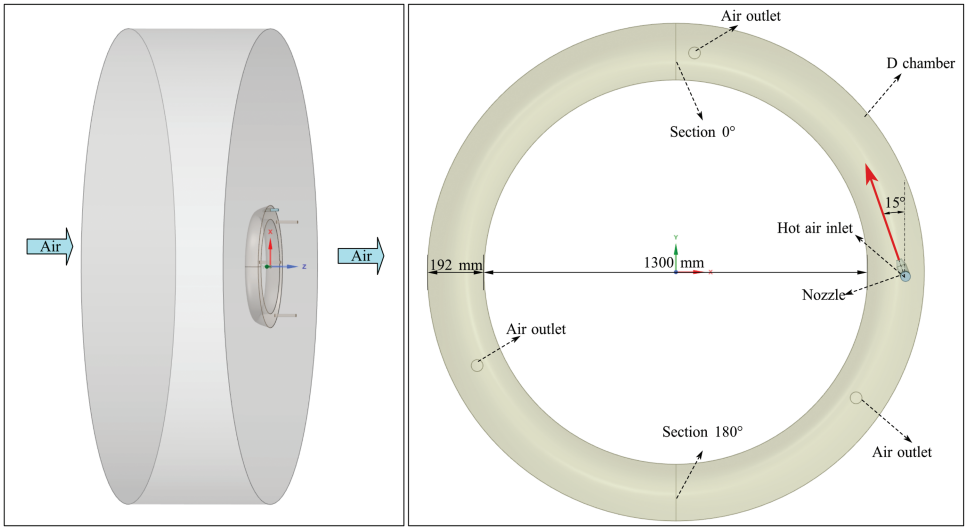

Figure 1: Model of the computational domain

Four comparative analysis configurations all use D-chambers with identical geometric dimensions. The inner-ring diameter the D-chamber is 1.3 m, the outer-ring diameter is 1.684 m, and the cross-sectional area is 0.029 m^2 for the D-chamber. The bleed air temperature is 533°C, and the bleed air mass flow rate ranges from 0.02 to 0.12 kg/s, yielding a nozzle jet exit velocity range from 98 to 375 m/s. The outlet is defined as a pressure boundary condition with an exhaust pressure of 96,500 Pa. The external flow field consists of dry air at a constant freestream velocity, with an ambient temperature of −6.7°C. The exhaust boundary of this field is also maintained at a constant pressure of 96,500 Pa.

Nozzle optimization is critical for improving heat transfer efficiency and achieving a more uniform surface temperature distribution in the SHAI system. Elliptical nozzles, due to their asymmetric geometry, effectively enhance turbulence and improve mixing efficiency. The multi-orifice nozzle design facilitates heat source dispersion, preventing local thermal concentrations and promoting a homogeneous thermal field. Incorporating a diffuser downstream of the nozzle facilitates pre-ejection deceleration of the hot airflow, ensuring better velocity matching with the ambient airflow. As shown in Fig. 2, four distinct nozzle designs were evaluated in this study, all sharing a 15° injection angle and a total outlet area of 0.000317 m^2. Specifically, Nozzle type 1 is a conical single-orifice baseline configuration. Nozzle type 2 is a modification of type 1, featuring a petal-shaped diffuser attached to its outlet, with a diffuser outlet area is 0.002652 m^2. Nozzle type 3 features a dual-elliptical-orifice design, incorporating two longitudinally aligned elliptical orifices, each with an area of 0.0001585 m^2 and an aspect ratio of 3:1. Nozzle type 4 adopts a quad-elliptical-orifice configuration, with four longitudinally arranged elliptical orifices, each with an area of 0.0000793 m^2 an aspect ratio of 3:1.

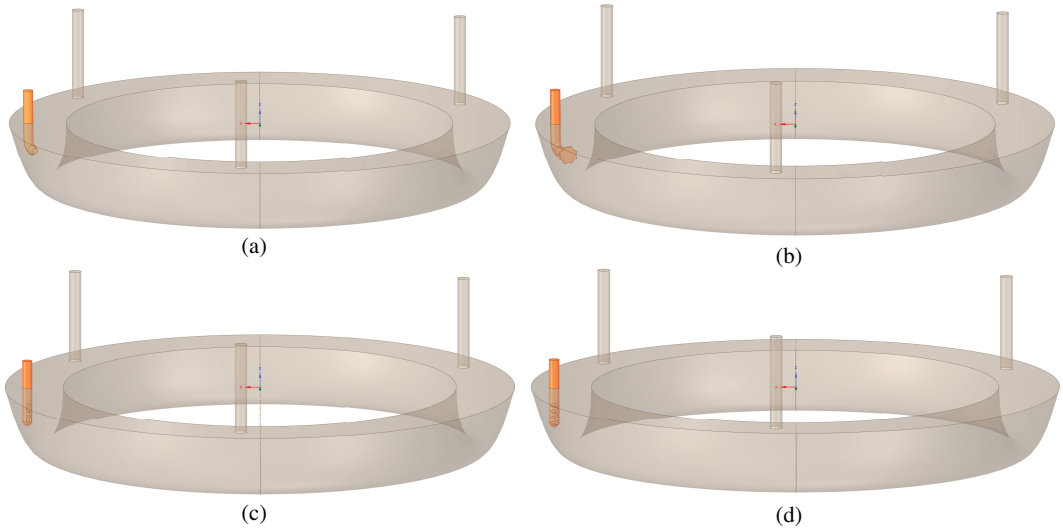

Figure 2: Four nozzle configurations: (a) type 1: conical single-orifice nozzle; (b) type 2: diffuser-equipped nozzle; (**c**) type 3: elliptical dual-orifice nozzle; (**d**) type 4: elliptical quad-orifice nozzle

2.2 Numerical Method

Numerical analyses were performed using ANSYS Fluent 2022. The three-dimensional, steady-state, viscous Navier–Stokes equations were solved to characterize the internal hot air flow field and wall temperature distribution within the D-chamber. A pressure-based coupled solver was employed, with the k-ω Shear Stress Transport (SST) turbulence model selected to resolve turbulent flow dynamics. Spatial discretization utilized second-order upwind schemes, and the SIMPLEC algorithm was applied for pressure–velocity coupling. The working fluid in this study is dry air, modeled as a compressible ideal gas with constant thermal conductivity, and the Sutherland viscosity model was incorporated to account for temperature-dependent viscosity effects. Hybrid initialization method is used to establish enhanced physical consistency initial fields by propagating prescribed boundary conditions across the entire domain.

Polyhedral mesh elements were generated using ANSYS Meshing, subdividing the computational domain into three regions: the nozzle region, the D-chamber region, and the external airflow region, as shown in Fig. 3. A conjugate heat transfer model with strong coupling was applied to resolve thermal interactions between the D-chamber region and the external airflow region. The mesh was uniformly generated across three regions, incorporating 20 boundary layers with near-wall Y+ values controlled at approximately 1 to ensure accurate resolution of viscous effects near the wall.

As presented in Table 1, five distinct mesh sizes were evaluated to ensure mesh independence. Key parameters within the D-chamber, including the chamber mainstream average velocity (v_b), average temperature of the lip surface (T_{sur}), maximum temperature of the lip surface (T_{max}), and minimum temperature of the lip surface (T_{min}), exhibited stability when the mesh count exceeded 10 million cells. To balance computational accuracy and efficiency, a total mesh size of approximately 10 million cells was selected for subsequent simulations.

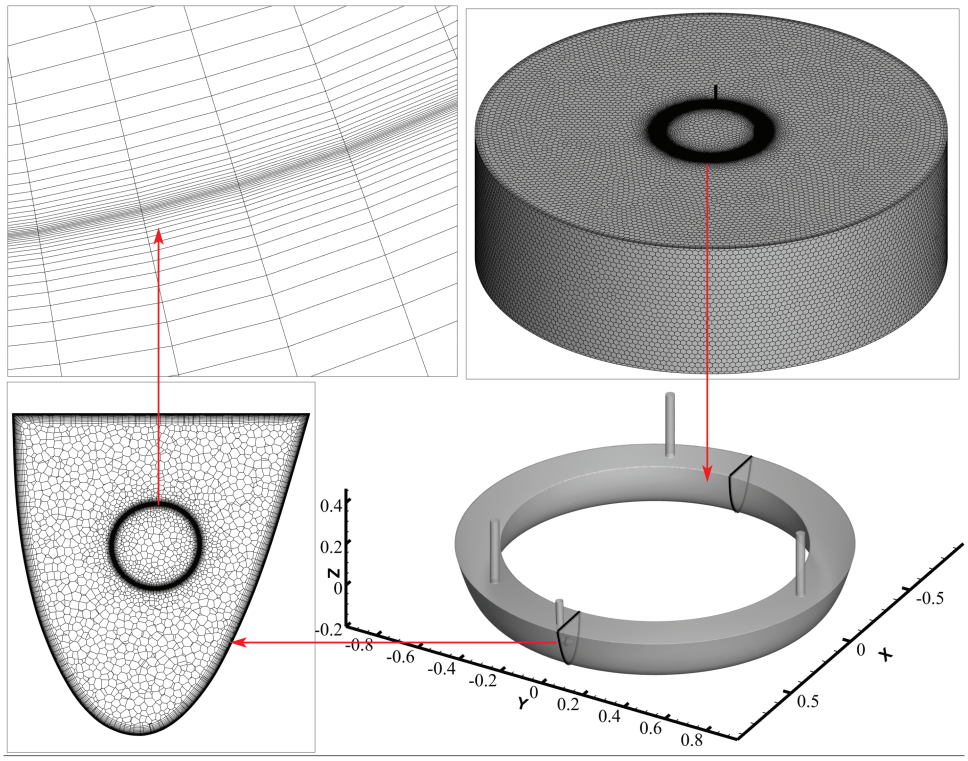

Figure 3: Mesh model

Table 1: Mesh independence analysis

Mesh size	v_b (m/s)	T_{sur} (°C)	T_{max} (°C)	T_{min} (°C)
2,586,024	66.6	314.6	373.6	290.6
4,857,588	66.7	314.3	364.8	288.2
7,212,235	66.3	313.1	358.6	286.7
9,844,718	66.1	312.7	352.7	285.8
12,577,792	66.1	312.6	352.4	285.6

2.3 Governing Equations and Data Reduction

In the fluid domain, the steady-state flow is governed by the continuity, momentum, and energy equations, presented in Eqs. (1)–(3).

$$\frac{\partial}{\partial \mathrm{x}_i}\left(\rho u_i\right)=0, \tag{1}$$

$$\frac{\partial}{\partial \mathrm{x}_j}\left(\rho u_i u_j\right)=-\frac{\partial p}{\partial x_i}+\frac{\partial \tau_{ij}}{\partial x_j}, \tag{2}$$

$$\frac{\partial}{\partial \mathrm{x}_i}\left(u_i\left(\rho E+p\right)\right)=\frac{\partial}{\partial \mathrm{x}_i}\left(k_{eff}\frac{\partial T}{\partial x_i}\right), \tag{3}$$

where u_i represents the total velocity vector, E stands for total energy, τ_{ij} denotes the stress tensor, and k_{eff} represents the effective thermal conductivity.

In the solid region, the steady-state energy transfer equation is given in Eq. (4), where k_{sl} signifies the thermal conductivity of a solid material.

$$\frac{\partial}{\partial x_i}\left(k_{sl}\frac{\partial T}{\partial x_i}\right)=0, \tag{4}$$

The CFD-predicted Nu_{ave} is calculated using Eq. (5):

$$Nu_{ave}=\frac{hd_h}{k}, \tag{5}$$

here, h is the average convective heat transfer coefficient, defined by Eq. (6) and d_h is the hydraulic diameter of the D-chamber defined by Eq. (7):

$$h=\frac{Q_w}{T_w-T_b}, \tag{6}$$

$$d_h=\frac{4A_D}{C}. \tag{7}$$

Q_w denotes the heat flux at the lip surface wall of the D-chamber, T_w is the corresponding wall temperature, and T_b is the mass-weighted average temperature of the air within the D-chamber. A_D is the cross-sectional area of the D-chamber, and C is the wetted perimeter of the chamber cross-section.

The system entrainment efficiency, ER, is defined as Eq. (8):

$$ER=\frac{G_s}{G_p}, \tag{8}$$

here, G_s denotes the secondary flow mass flow rate, while G_p represents the primary flow mass flow rate of the bleed air from the aero-engine.

2.4 Validation

The averaged Nusselt number (Nu_{ave}) serves as a critical indicator of overall thermal performance in the anti-icing chamber. Existing research has established empirical correlations based on experimental data and numerical methods to characterize this parameter. To validate the accuracy and reliability of the numerical method, the Nu_{ave} of the D-chamber for the conical single-orifice nozzle was compared against the empirical correlation as shown in Eq. (9) [9] across a Reynolds number (Re) range from 1×10^6 to 6×10^6.

The model adopts a conical single-orifice nozzle with a nozzle angle of 15°. As shown in Fig. 4, within the Re range examined in this study, the maximum relative error of the Nu_{ave} between CFD-predicted values and the empirical correlation is 2.52%, demonstrating strong agreement and confirming the model's credibility.

$$Nu_{ave}=0.0298Re^{0.8}Pr^{1/3}. \tag{9}$$

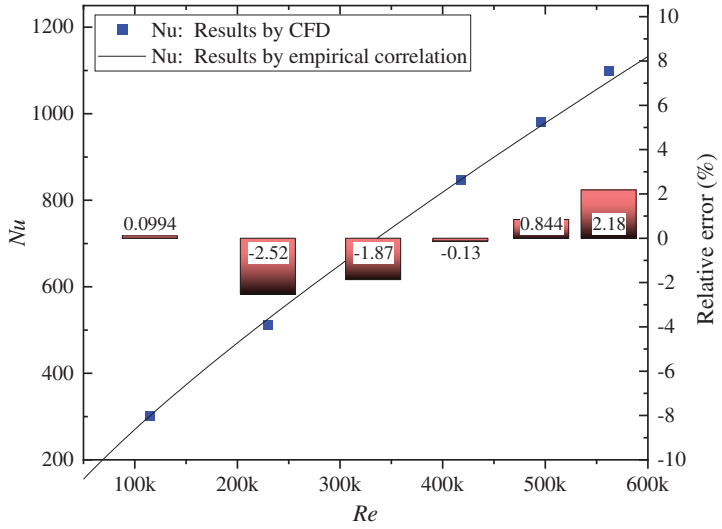

Figure 4: Model validation

3 Results and Discussion

This study comparatively analyzes four nozzle configurations: conical single-orifice nozzle (type 1), diffuser-equipped nozzle (type 2), elliptical dual-orifice nozzle (type 3), and elliptical quad-orifice nozzle (type 4). All analysis cases share identical nozzle exit area (throat area for the diffuser-equipped nozzle), jet angle, geometric parameters of the D-chamber, injected mass flow range, exhaust pressure, and the ambient condition to ensure comparability.

3.1 Effect of Nozzle Configurations on the Entrainment Characteristic

The nozzle design is a critical determinant of hot air jet entrainment efficiency. It directly influences jet momentum, turbulence intensity, mixing path, and energy distribution, thereby governing both entrainment effectiveness and mixing efficiency. As shown in Fig. 5a, under identical injection air flow rates, the internal circulation flow rates within the D-chamber decrease in the following order: conical single-orifice nozzle > elliptical quad-orifice nozzle > elliptical dual-orifice nozzle > diffuser-equipped nozzle. Notably, the entrainment efficiency of the diffuser-equipped nozzle is remarkably lower than that of the other three types. As shown in Fig. 5b, all nozzle types exhibit nonlinear entrainment efficiency trends, generally following a pattern of initial increase followed by a decrease with the increasing injection flow rates. Regarding peak efficiency, the conical single-orifice nozzle performs the best among all nozzle types, whereas the diffuser-equipped nozzle shows the lowest efficiency, which is 16.4%–18.1% lower than that of the conical type.

Fig. 6 illustrates the velocity contour near the nozzle outlet of the D-chamber cross-section. Observations show that for the conical single-orifice nozzle (type 1), its axisymmetric geometry concentrates the jet momentum along the axial direction. This reduces energy loss from lateral diffusion, and enhancing penetration capability, which directly correlates with its highest entrainment efficiency. By contrast, integrating a diffuser downstream (type 2) induces a velocity drop in the diffuser section, causing premature kinetic energy decay that weakens both penetration and entrainment performance. For the elliptical multi-orifice nozzles (type 3 and type 4), the jet diffuses rapidly along the elliptical major axis, leading to kinetic energy dissipation at the outlet. Additionally, mutual interference among

multiple jets exacerbates energy loss, shortening the core jet region, and diminishing penetration capability compared to the single-orifice nozzle. Although multiple jets increase the contact area between the primary and secondary flow, thereby enhancing momentum exchange and fluid mixing to promote entrainment, their overall entrainment efficiency remains inferior to that of the conical single-orifice nozzle.

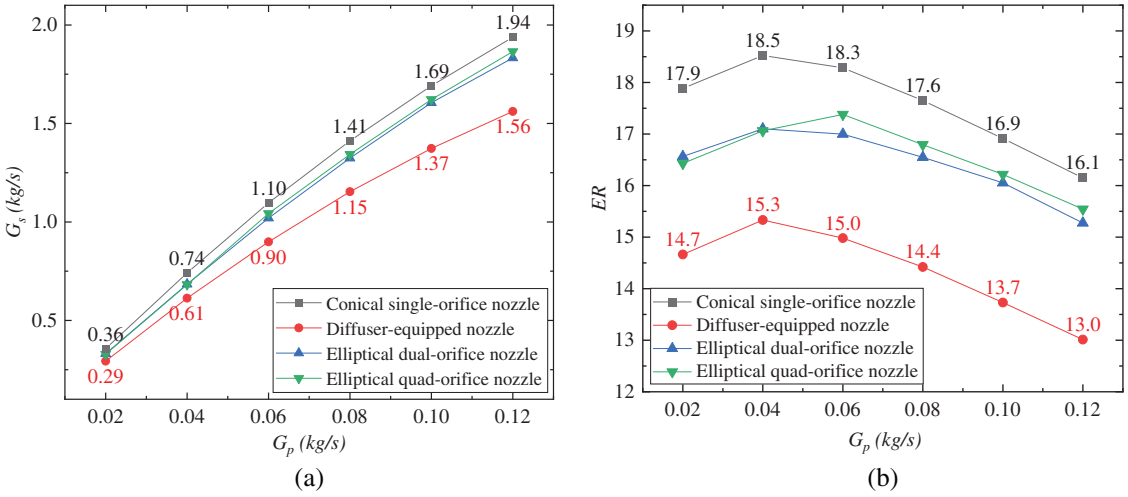

Figure 5: Effect of nozzle configurations on entrainment characteristics: (**a**) Secondary flow mass flow rate; (**b**) Entrainment efficiency

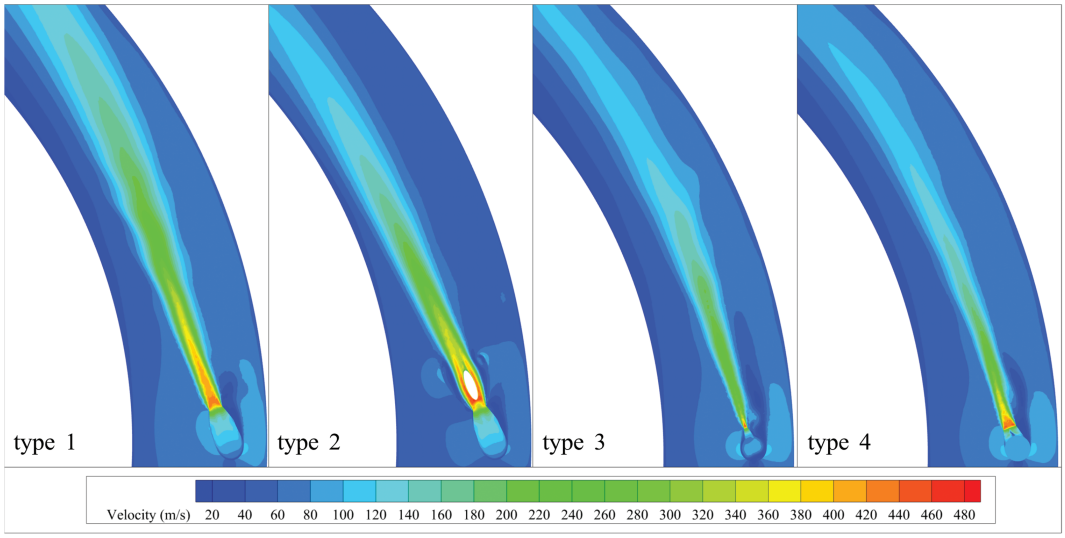

Figure 6: Velocity contour of the D-chamber cross-section near the nozzle outlet

In summary, with identical outlet area and injection angle, the conical single-orifice nozzle effectively suppresses turbulence and enhances momentum transfer efficiency due to its highly concentrated jet, thereby achieving optimal overall entrainment performance.

3.2 Effect of Nozzle Configurations on the Flow Resistance Characteristic

Fig. 7 illustrates a comparative analysis of the bleed pressure requirements for the four nozzle types. The analysis results indicate that, under identical inlet mass flow rates, the system pressure drops among nozzle configurations are not significant, ordered from highest to lowest as follows: elliptical quad-orifice nozzle, elliptical dual-orifice nozzle, conical single-orifice nozzle, and diffuser-equipped nozzle. Notably, the first three nozzle types exhibit closely aligned flow resistance values, whereas the diffuser-equipped nozzle demonstrates a marked reduction in total pressure drop. This phenomenon arises from results from premature decay of the mainstream kinetic energy within the diffuser, which diminishes entrainment efficiency and results in a substantially lower circulation velocity inside the anti-icing cavity compared to the other three nozzles (shown in Fig. 8), thereby producing the lowest circulation flow resistance. Fig. 8 also shows that the conical single-orifice nozzle case achieves the highest circulation velocity in the D-chamber, but the velocity discrepancy is not significant relative to multi-orifice nozzles.

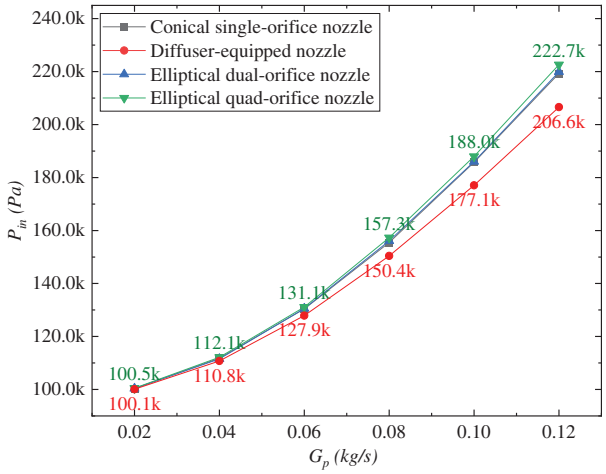

Figure 7: The bleed pressure requirement of the SHAI system

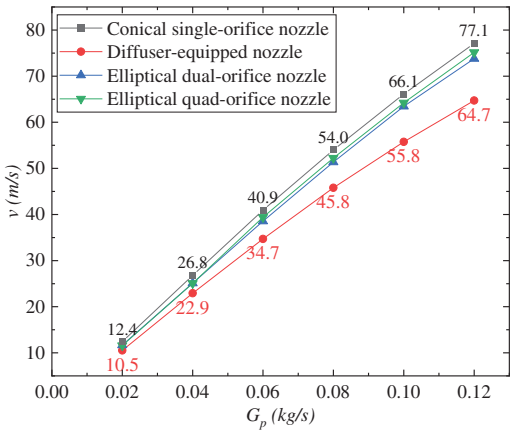

Figure 8: Circulation velocity of the working fluid in the D-chamber

Fig. 9 illustrates the streamline of the flow field in the D-chamber. Compared with the conical single-orifice nozzle (type 1), the diffuser-integrated nozzle (type 2) and elliptical multi-orifice nozzles

(type 3 and type 4) exhibit more pronounced circumferential diffusion characteristics at the outlet. While this feature enhances mixing between hot and ambient cold air, it results in momentum loss along the jet direction, shortening the core jet region length and weakening the entrainment effect. Multi-orifice nozzles disperse high-speed injected air through small orifices, effectively expanding the mixing zone and improving thermal mixing efficiency between hot and cold air. However, the multiple jets nozzles interfere mutually, increasing turbulence intensity within the D-chamber and thereby elevating system circulation flow resistance. Consequently, although the circulation velocity in the multi-orifice nozzle chamber is slightly lower than that of conical single-orifice nozzle, its overall pressure drop is marginally higher.

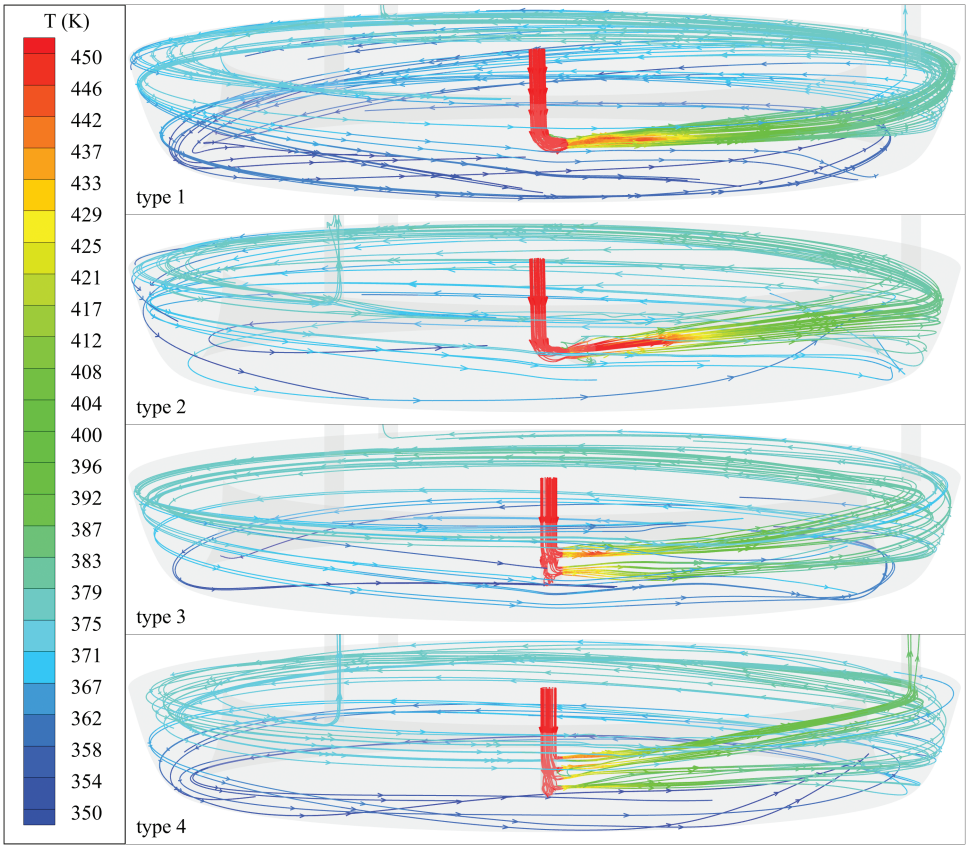

Figure 9: Streamline diagram in the D-chamber

3.3 Effect of Nozzle Configurations on the Hot-Cold Spot Distribution Characteristic

As shown in Fig. 10a,b, the nozzle configuration significantly influences the temperatures of both cold spots and hot spots on the lip surface. In terms of hotspot suppression, the other three nozzle types all exhibit improvements compared to the conical single-orifice nozzle, with the quad-orifice nozzle demonstrating the most pronounced effect, achieving a hotspot temperature reduction of up to 17.6°C compared to the conical single-orifice design. For cold spot suppression, the quad-orifice nozzle again demonstrates the best performance, followed by the diffuser-integrated nozzle, while the conical single-orifice nozzle still exhibits the lowest cold spot temperature. As shown in Fig. 10b, the

elliptical four-hole nozzle can increase the cold spot temperature by up to 7.2°C compared to the conical single-hole nozzle.

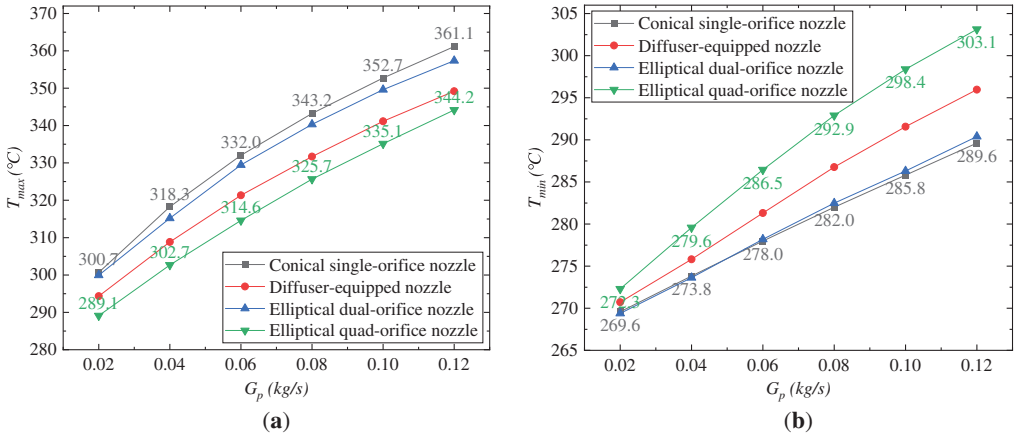

Figure 10: Hot-cold spots distribution characteristics of the lip surface: (**a**) maximum temperature of the lip surface; (**b**) minimum temperature of the lip surface

Fig. 11 illustrates the temperature distribution on the lip surface of the anti-icing D-chamber. As shown in the figure, hot spots are mainly distributed in the wall region subjected to direct jet impingement while the cold spots are mainly distributed on the inner-ring wall of the D-chamber. The formation of cold spots is primarily attributed to the centrifugal effect of the flow within the annular channel. This effect results in higher fluid velocity on the outer-ring side of the D-chamber than that on the inner-ring side, and simultaneously, the convective heat transfer intensity on the outer-ring side is also higher. Under various nozzle configurations, the outer-ring side wall of the D-chamber consistently exhibits a notably higher temperature than the inner ring wall, with all cold spots localized on the inner duct wall. The figure further shows that that the conical single-hole nozzle (type 1) induces the most pronounced wall impingement and centrifugal effects, leading to the largest hot spot area and peak hot spot temperatures. By integrating a diffuser at the nozzle outlet (type 2) or adopting multi-orifice injection (types 3 and 4), the incident energy can be dispersed, all of which can mitigate wall impingement effects, reduce hot spot temperatures, and decrease hot spot areas.

Fig. 12 illustrates the temperature contours and velocity vector of the local cross-section adjacent to the nozzle in the D-chamber. Within the annular channel, the fluid velocity exhibits significant radial variation, with the velocity on the outer-ring side exceeding that on the inner-ring side. The main fluid tends to be extruded outward due to inertia, causing the trailing segment of the jet to deflect toward the outer-ring side. This effect is most pronounced for the conical single-hole nozzle (type 1), where distinct temperature stratification is observed in the inner-ring region of the annular channel. Compared with the conical single-orifice nozzle case, the high-temperature envelopes of the jet flow at multi-orifice nozzles (type 3 and type 4) exits are markedly reduced in spatial extent. This reduction can be attributed to their highly diffused flow trajectories, which enhances the mixing efficiency between hot and cold air. It also enables rapid heat diffusion, thereby reducing the temperature and spatial extent of the high-temperature zone. The diffuser-equipped nozzle (type 2) partially restores static pressure within the diffuser, resulting in a relatively elevated exit temperature compared to other nozzle configurations. This nozzle induces premature jet dispersion, reduces the jet velocity, and thereby effectively weakens the wall impingement intensity of the jet. In contrast to the concentrated jet of the conical single-orifice nozzle (type 1), such premature dispersion significantly expands the

mixing interface, effectively enhancing the mixing efficiency between the injected hot air and the chamber's circulating air. This mechanism inherently inhibits the genesis of thermal inhomogeneities, encompassing both hot spots and cold spots.

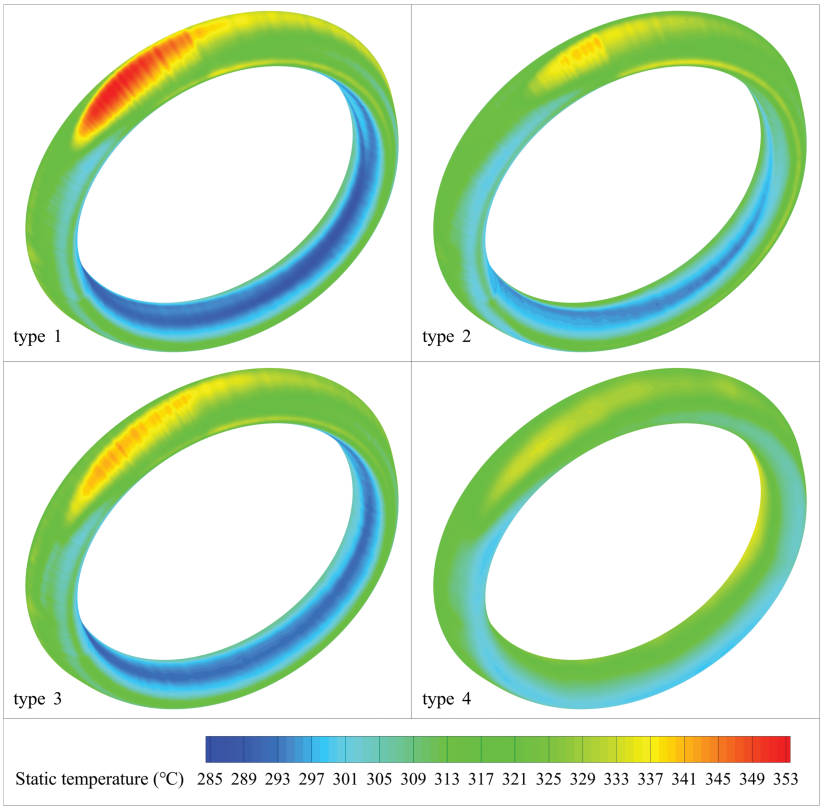

Figure 11: Temperature contour plot of the lip surface under four nozzle configuration cases

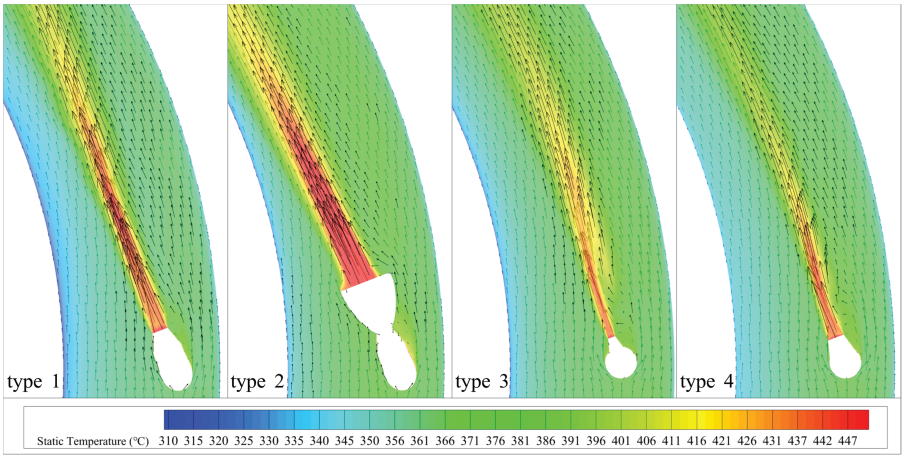

Figure 12: Velocity vector diagrams of the cross-section near the nozzle region

In general, compared with the type 1 nozzle case, types 2, 3, and 4 all demonstrate the capability to mitigate the thermal inhomogeneity phenomenon on the lip surface. Notably, type 4 exhibits the

optimal suppression effect: compared with type 1, it reduces the temperature difference between hot and cold spots by 24.8°C, achieving an overall reduction of 34.7%.

3.4 Effect of Nozzle Configurations on the Heat Transfer Characteristic

Fig. 13 illustrates the analysis results of the average temperature on the D-chamber lip surface. Within the analyzed bleed flow range, the elliptical quad-orifice nozzle consistently yields a higher lip surface temperature (T_{sur}), with this trend being particularly pronounced at higher bleed mass flow rates. Compared to the conical single-orifice nozzle cases, the surface average temperature exhibits an increase of up to 3°C. The diffuser-equipped nozzle exhibits the lowest T_{sur} among the four configurations.

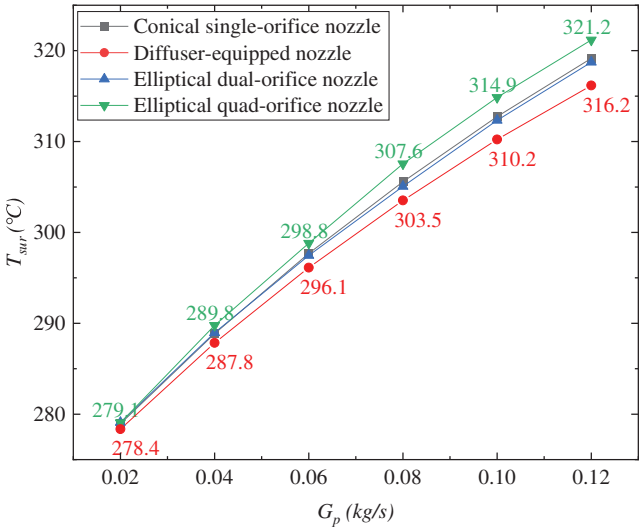

Figure 13: Average temperature result of the D-chamber lip surface

As illustrated in Fig. 14, the nozzle configuration exerts a significant influence on the average convective heat transfer coefficient (h) of the D-chamber lip surface. The conical single-orifice nozzle exhibits the highest h value, whereas the diffuser-equipped nozzle case demonstrates the lowest h. This finding is generally consistent with the trends of the ER and v observed in Figs. 5b and 8 for each nozzle configuration. Evidently, the circulating flow velocity within the D-chamber plays a pivotal role in enhancing the internal average convective heat transfer performance.

The analysis results of the Nu_{ave} in Fig. 15 reveal that, under identical jet angle, nozzle outlet area, and D-chamber geometries, the influence of nozzle configuration on the Nu_{ave} of the D-chamber lip wall is relatively insignificant. The CFD predictions of the Nu_{ave} for various nozzle configurations demonstrate good agreement with Eq. (9), with the maximum discrepancy across all configurations constrained within 5.48%. Notably, this figure also illustrates significant deviations between the Nu_{ave} analysis results of the four nozzle configurations and Eq. (10) [15]. This discrepancy arises primarily because the two empirical correlations adopt different jet angles and D-chamber geometrisc parameters, whereas this study uses the same jet angles and D-chamber geometries as those in the literature source of Eq. (9). Evidently, the design of the jet angle and D-chamber geometries exerts a significant influence on the Nu_{ave} of the D-chamber lip wall.

$$Nu_{ave} = 0.0055 Re^{0.947} Pr^{1/3}. \tag{10}$$

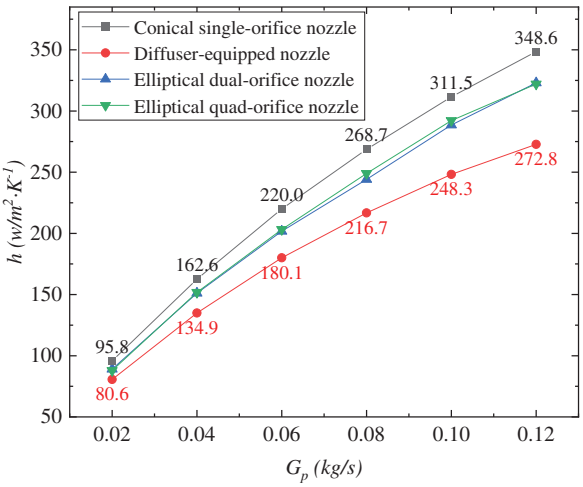

Figure 14: Average convective heat transfer coefficient of the D-chamber lip wall

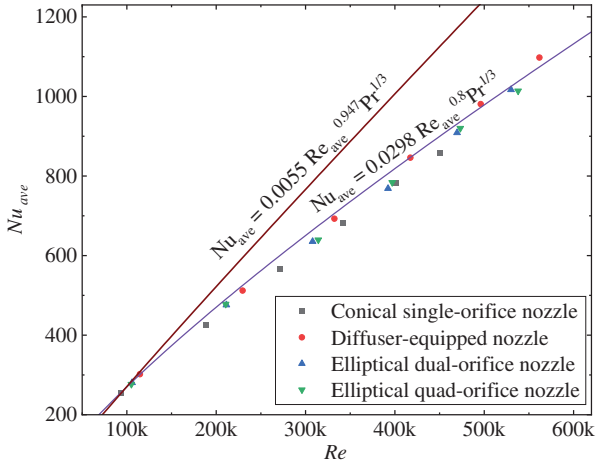

Figure 15: Average nusselt number of the D-chamber lip wall

4 Conclusions

This research employs CFD method to comparatively study the flow and heat transfer characteristics within the SHAI chamber of the aero-engine with four distinct nozzle configurations. The investigation focuses on the effects of nozzle geometry on entrainment efficiency, system flow resistance, surface hot-cold spot distribution, and average heat transfer performance of the SHAI chamber. The following conclusions were obtained:

The conical single-orifice nozzle generates a concentrated jet with optimal entrainment efficiency. The addition of a diffuser downstream of the nozzle causes premature kinetic energy dissipation prior to interaction with the secondary flow, significantly reducing entrainment capability. Among the four nozzle types, the diffuser-equipped design exhibits the poorest entrainment performance, with entrainment efficiency 16.4%–18.1% lower than that of the conical single-orifice nozzle across the analyzed bleed air flow range.

Compared to the conical single-orifice nozzle, the other three nozzle configurations effectively suppress hot and cold spots on the aero-engine lip surface, with the elliptical quad-orifice nozzle demonstrating the best suppression effect. At a bleed flow rate of 0.12 kg/s, this nozzle type reduces hot and cold spot temperature differential by 34.7% relative to the conical single-orifice nozzle case. Furthermore, the quad-orifice nozzle achieves the highest average lip surface temperature under matched flow conditions, solidifying its status as the optimal configuration in this comparative study.

Under identical D-chamber geometry and jet angle conditions, the influence of nozzle configuration on Nu_{ave} within the D-chamber remains insignificant. Across the Re range investigated in this study, the maximum deviations of all nozzle types from empirical correlation predictions do not exceed 5.48%.

This study focuses on the effects of nozzle configurations on the flow and heat transfer characteristics inside the swirling anti-icing chamber, maintaining consistent D-chamber geometry across all nozzle configurations. The findings reveal that nozzle structure mainly influences the distribution of hot and cold spots. Optimizing nozzle design can improve the temperature uniformity of the lip surface. However, the nozzle type exhibits a very limited effect on the Nu inside the swirling anti-icing chamber. Future work will investigate the impact of D-chamber geometric parameters on the anti-icing system performance of the aero-engine.

Acknowledgement: This work was also supported by Hunan Provincial Natural Science Foundation, grant number 2022JJ30422; Education Department of Hunan Province, China, grant number 23B0660.

Funding Statement: This research was funded by Education Department of Hunan Province, China, grant number 23A0504; Shenyang Key Laboratory of Aircraft Icing and Ice Protection, grant number XFX20220303; The APC was funded by Hunan Province Engineering Research Center of Digital Twin for Construction Machinery, grant number 2023TP2057.

Author Contributions: Conceptualization, Yi Tu and Yuan Wu; methodology, Yi Tu; software, Yi Tu; validation, Yi Tu and Bin Zeng; formal analysis, Yi Tu; investigation, Yi Tu and Yu Zeng; resources, Wen Liu; data curation, Yi Tu and Yuan Wu; writing—original draft preparation, Yi Tu; writing—review and editing, Songrong Luo and Bin Zeng; visualization, Yi Tu; supervision, Yuan Wu; project administration, Yi Tu; funding acquisition, Yi Tu and Yuan Wu. All authors reviewed the results and approved the final version of the manuscript.

Availability of Data and Materials: The authors confirm that the data supporting the findings of this study are available within the article.

Ethics Approval: Not applicable.

Conflicts of Interest: The authors declare no conflicts of interest to report regarding the present study.

Abbreviations

CFD	Computational Fluid Dynamics
HAI	Hot air Anti-Icing
SHAI	Swirl Hot air Anti-Icing

References

1. Zheng M, Guo Z, Dong W, Guo X. Experimental investigation on ice accretion on a rotating aero-engine spinner with hydrophobic coating. Int J Heat Mass Transf. 2019;136(1776):404–14. doi:10.1016/j.ijheatmasstransfer.2019.02.104.
2. Ranaudo RJ, Batterson JG, Reehorst AL, Bond TH, O'Mara TM. Effects of horizontal tail ice on longitudinal aerodynamic derivatives. J Aircr. 1991;28(3):193–9. doi:10.2514/3.46012.
3. Bennani L, Trontin P, Radenac E. Numerical simulation of an electrothermal ice protection system in anti-icing and deicing mode. Aerospace. 2023;10(1):75. doi:10.3390/aerospace10010075.
4. Jiang X, Wang Y. Studies on the electro-impulse de-icing system of aircraft. Aerospace. 2019;6(6):67. doi:10.3390/aerospace6060067.
5. Elangovan R, Olsen R. Analysis of layered composite skin electro-thermal anti-icing system. In: 46th AIAA Aerospace Sciences Meeting and Exhibit. Reno, NV, USA: AIAA; 2008. AIAA2008–446. doi:10.2514/6.2008-446.
6. Khai LC, Ismail MA, Azam Q, Mazlan NM. Experimental study on aerodynamic performance of nacelle lip-skin bias flow. J Mech Sci Technol. 2020;34(4):1613–21. doi:10.1007/s12206-020-0323-0.
7. Liu Y, Xu R, Luo N, Liu Y, Wu Y, Yu B, et al. All-day anti-icing/de-icing coating by solar-thermal and electric-thermal effects. Adv Mater Technol. 2021;6(11):2100371. doi:10.1002/admt.202100371.
8. Chu Z, Jiao W, Huang Y, Ding G, Zhong X, Yan M, et al. FDTS-modified SiO_2/rGO wrinkled films with a micro-nanoscale hierarchical structure and anti-icing/deicing properties under condensation condition. Adv Mater Interfaces. 2020;7(1):1901446. doi:10.1002/admi.201901446.
9. Tu Y, Wu Y, Zeng Y. Study of flow and heat transfer in an ejector-driven swirl anti-icing chamber. Fluid Dyn Mater Process. 2024;20(5):989–1014. doi:10.32604/fdmp.2024.045624.
10. Saeed F. Numerical simulation of surface heat transfer from an array of hot-air jets. J Aircr. 2008;45(2):700–14. doi:10.2514/1.33489.
11. Guo Z, Guo X, Yang Q, Dong W. Heat transfer characteristics of unexpanded jet impingement in piccolo hot air anti-icing chamber. Appl Therm Eng. 2022;200(1):117540. doi:10.1016/j.applthermaleng.2021.117540.
12. Munas FR, Kok Hwa Y, Yusoff N, Muzathik AM, Ismail MA. Integrating ice protection and noise abatement systems for aircraft application: a review. Pertanika J Sci Technol. 2023;31(6):2667–87. doi:10.47836/pjst.31.6.02.
13. Rosenthal H, Nelepovitz D. Performance of a new nose-lip hot-air anti-icing concept. In: 21st Joint Propulsion Conference; 1985 Jul 8–10; Monterey, CA, USA. doi:10.2514/6.1985-1117.
14. Chilukuri K. Curved duct flow and heat transfer in engine anti-icing. In: 2018 AIAA Aerospace Sciences Meeting; 2018 Jan 8–12; Kissimmee, Fl, USA. doi:10.2514/6.2018-0406.
15. Ismail MA, Wang J. Effect of nozzle rotation angles and sizes on thermal characteristic of swirl anti-icing. J Mech Sci Technol. 2018;32(9):4485–93. doi:10.1007/s12206-018-0845-x.
16. Anderson M. Shielded swirl versus piccolo tube inlet thermal anti-icing system. In: ASME Turbo Expo 2019: Turbomachinery Technical Conference and Exposition; 2019 Jun 17–21; Phoenix, AZ, USA. New York, NY, USA: American Society of Mechanical Engineers; 2019. V001T01A016. doi:10.1115/gt2019-90992.
17. Liu Y, Yi X. Investigations on hot air anti-icing characteristics with internal jet-induced swirling flow. Aerospace. 2024;11(4):270. doi:10.3390/aerospace11040270.
18. Mark R, Georgia C, Daniel S. Method and apparatus for aircraft anti-icing. United States patent US 34756408A. 2011 Nov 22.
19. Michael SV. Hot air injection for swirling rotational anti-icing system. United States patent US 09,422,918. 2001 Jul 31.
20. Radhakrishna C. Passive control of hot air injection for swirling rotational type anti-icing system. United States patent US 09,426,411. 2002 Mar 12.

21. Joel HF, Lubomir AR. Injector nozzle configuration for swirl anti-icing system. United States patent US 14,836,015. 2020 Jul 28.
22. Su Q, Chang S, Zhao Y, Zheng H, Dang C. A review of loop heat pipes for aircraft anti-icing applications. Appl Therm Eng. 2018;130(1):528–40. doi:10.1016/j.applthermaleng.2017.11.030.
23. Yang Q, Zheng H, Guo X, Dong W. Experimental validation and tightly coupled numerical simulation of hot air anti-icing system based on an extended mass and heat transfer model. Int J Heat Mass Transf. 2023;217(5):124645. doi:10.1016/j.ijheatmasstransfer.2023.124645.
24. Li L, Liu Y, Tian L, Hu H, Hu H, Liu X, et al. An experimental study on a hot-air-based anti-/de-icing system for aero-engine inlet guide vanes. Appl Therm Eng. 2020;167:114778. doi:10.1016/j.applthermaleng.2019.114778.
25. Croce G, Habashi W, Guevremont G, Tezok F. 3D thermal analysis of an anti-icing device using FENSAP-ICE. In: 36th AIAA Aerospace Sciences Meeting and Exhibit; 1998 Jan 12; Reno, NV, USA. doi:10.2514/6.1998-193.
26. Ismail MA, Abdullah MZ. Applying computational fluid dynamic to predict the thermal performance of the nacelle anti-icing system in real flight scenarios. Indian J Sci Technol. 2015;8(30):1–8. doi:10.17485/ijst/2015/v8i30/86058.
27. Bu X, Lin G, Shen X, Hu Z, Wen D. Numerical simulation of aircraft thermal anti-icing system based on a tight-coupling method. Int J Heat Mass Transf. 2020;148(3):119061. doi:10.1016/j.ijheatmasstransfer.2019.119061.
28. Yang Q, Guo X, Zheng H, Dong W. Single- and multi-objective optimization of an aircraft hot-air anti-icing system based on Reduced Order Method. Appl Therm Eng. 2023;219(8):119543. doi:10.1016/j.applthermaleng.2022.119543.
29. Chen N, Yi X, Wang Q, Chai D, Li C. A literature review on numerical simulation of thermal anti-icing. Aerospace. 2025;12(2):83. doi:10.3390/aerospace12020083.